ELSEVIER

Chemical Engineering Journal 90 (2002) 61–76

Chemical Engineering Journal

www.elsevier.com/locate/cej

Development of the kinetic model of platinum catalyzed ammonia oxidation in a microreactor

E.V. Rebrov, M.H.J.M. de Croon, J.C. Schouten*

Laboratory of Chemical Reactor Engineering, Schuit Institute of Catalysis, Eindhoven University of Technology, P.O. Box 513, 5600 MB Eindhoven, The Netherlands

Abstract

The ammonia oxidation reaction on supported polycrystalline platinum catalyst was investigated in an aluminum-based microreactor. An extensive set of reactions was included in the chemical reactor modeling to facilitate the construction of a kinetic model capable of satisfactory predictions for a wide range of conditions (NH_3 partial pressure, 0.01–0.12 atm; O_2 partial pressure, 0.10–0.88 atm; temperature, 523–673 K; contact time, 0.3–0.7 ms). The elementary surface reactions used in developing the mechanism were chosen based on the literature data concerning ammonia oxidation on a Pt catalyst. Parameter estimates for the kinetic model were obtained using multi-response least squares regression analysis using the isothermal plug-flow reactor approximation. To evaluate the model, the behavior of a microstructured reactor was simulated by means of a complete Navier–Stokes model accounting for the reactions on the catalyst surface and the effect of temperature on the physico–chemical properties of the reacting mixture. In this way, the effect of the catalytic wall temperature non-uniformity and the effect of a boundary layer on the ammonia conversion and selectivity were examined. After further optimization of appropriate kinetic parameters, the calculated selectivities and product yields agree very well with the values actually measured in the microreactor.

Keywords: Ammonia oxidation; Kinetic model; Platinum; Microreactor; Navier–Stokes

1. Introduction

Characteristic dimensions of reaction channels in microreactors in the range of 100–300 μm open new possibilities for measuring intrinsic reaction kinetics [1,2]. Furthermore, due to the very large surface-to-volume ratio in a microreactor and a high thermal conductivity of the reactor material, efficient temperature control can be achieved, providing for near isothermal conditions even in case of strongly exothermic reactions [3]. Miniaturizing the chemical reactor makes it possible to avoid undesirable side effects of poor heat exchange, such as large times required to heat the inlet reactant gas and to quench the outlet product mixture. Finally, the velocity distribution is much more uniform in a microreactor enabling to achieve previously inaccessible residence times. Thus a micromachined reactor could be used as an efficient tool for the investigation of the fast kinetics of a reaction.

In this paper, we examine the low temperature kinetics of the ammonia oxidation on Pt catalyst. This reaction is considered as a classic example of a strongly exothermic, heterogeneous, catalytic reaction [4]. Due to the very fast kinetics of oxidation reactions, a direct experimental investigation of several reaction steps is difficult at realistic conditions. Therefore, simulation studies are needed, based on experimental data obtained in the low temperature region, to examine the reaction behavior. In addition to the investigation of the fundamental aspects of the intrinsic reaction kinetics, the direct catalytic oxidation of ammonia to nitrous oxide also holds great promise as a practical alternative to the currently used routes for N_2O production [5]. The process can be conducted autothermally at relatively low temperatures and very short contact times, due to the strong exothermicity and the very high reaction rates of the underlying oxidation reactions. Selectivity to nitrous oxide at low temperature was reported in the following order: Pt > Pd > Ni > Fe > W > Ti [6]. DeLaney and Manogue demonstrated that over unsintered 0.5% Pt/Al_2O_3 catalyst, the selectivity to N_2O was as high as 45% [7]. Later, Li and Armor showed that N_2O selectivity could reach 61% on Pt-ZSM-5 catalyst containing 2.55 wt.% Pt in a conventional fixed-bed reactor [8]. However, the latter is bound to a fatal loss of N_2O selectivity, when increasing the ammonia inlet concentration above 4 vol.%, leading to no further considerable improvement.

An understanding of the mechanism and the dynamics of the reaction are critical for process development. Several studies have focused their interest on the investigation of

* Corresponding author. Tel.: +31-40-247-3088; fax: +31-40-244-6653.
E-mail address: j.c.schouten@tue.nl (J.C. Schouten).
URL: http://www.chem.tue.nl/scr

1385-8947/02/$ – see front matter
PII: S1385-8947(02)00068-2

the mechanism of the ammonia oxidation [9–15]. Early work on NH_3 oxidation was reviewed by Il'chenko [6]. Later, several reviews [16–18] were published in attempt to compare different kinetic models concerning the reactions of NH_3 and oxygen on Pt surfaces, not mentioning a lot of original papers clearly beyond the scope of our present analysis. In the last 5 years, the mechanism of ammonia oxidative transformations was essentially revised based on recent experimental data which appear to be quite reliable, since they were obtained using in situ IRS, transient response technique, and isotope methods. At present, all reaction steps for most of the conditions are known fairly well at atmospheric and/or sub-atmospheric pressure. Despite of some uncertainties, a detailed mechanism, based on a large number of elementary reactions, can be drawn. For many of the reactions also their rate constants are accurately known. For some reactions, however, large uncertainties in the rate constants still exist. For example, for the key reaction step, i.e. NO desorption, Gorte et al. reported an activation energy of 154.7 kJ/mol [19], Pirug and Bonzel of 139.2 kJ/mol [20], whereas Sadhankar and Lynch of 54.3 kJ/mol [21]. This apparent discrepancy in activation energy for the same reaction may be attributed to the different Pt particle sizes in the catalysts used.

In spite of the fact that the size of the supported metal particle was considered earlier as another factor influencing the kinetics of the ammonia oxidation on platinum [7,14,22–24], none of the published mechanisms addressed this point. For example, a 5.5-fold increase in the turnover frequency (TOF) was reported, when the platinum loading was increased from 1.0 to 2.9 wt.% [22,23]. An explanation is based on the change of the Pt cluster size as a function of metal loading. An increase in the average size of the metal clusters or patches facilitates the formation of a favorable configuration of sites for the formation of the surface intermediates. The catalytic activity of stepped Pt $\{1\,1\,1\}$ was found to be greater than that of planar Pt $\{1\,1\,1\}$ [15]. This was attributed to a greater efficiency for O_2 dissociation on a stepped surface. It was also reported that the stoichiometry of oxygen chemisorption increases by a factor 2.7 with increasing platinum crystallite size [22,25]. This could also lead to an increase of the reaction rate if the oxygen adsorption is the rate-determining step in this system. Recently, we also demonstrated a two-fold increase in the TOF when the platinum loading was increased from 0.2 to 1.3 wt.% [26]. The increase in the reaction rate with the metal loading was explained by a rearrangement of the noble metal atoms into another geometrical configuration. Such process often requires a change in the basic reaction mechanism. It should be mentioned that the crystallite size effect was also observed on a Pt/Al_2O_3 catalyst in the NO reduction by hydrogen. The surface chemistry of this reaction can be considered as an integral part of that in the ammonia oxidation. The authors observed the striking increase in the TOF beyond the saturation concentration of the dispersed platinum phase [27].

A variation of the TOF for catalysts with platinum contents varying from 0.05 wt.% in a supported catalyst to 100% in a Pt monolith showed that there was a certain limit to the effect. Actually, the TOF only slightly changed with increasing Pt loading from 1.3 to 3.5 wt.% [26], whereas a further increase of the Pt loading above 3.5 wt.% did not cause any changes in the TOF.

The increase of supported platinum particle size led also to considerable changes in selectivity in the ammonia oxidation over a Pt/Al_2O_3 catalyst [7,22,26]. Large crystallites of 15.5 nm, for which over 98% of the surface atoms are plane atoms [28], exhibited low selectivity to nitrogen formation. Selectivity to nitrogen increased with decreasing platinum loading [22,26]. In fact, a change of the electronic properties of the Pt surface occurs as a result of the different size of the Pt clusters. This could point at various degrees of destabilization of the N–H bond in relation with chemisorption. The electron-rich sites partially dissociated N–H. Electron-poor sites could totally dissociate N–H. In such conditions very reactive atomic N species could interact to form N_2. This may explain large scattering of the literature data.

Based on aforementioned issues, one can conclude that an appropriate choice of the catalyst configuration is very important. At low platinum loadings, the catalyst consists mainly of isolated atoms [26]. Oxidation of ammonia on a single site is based on an Eley–Rideal mechanism. Even isolated dual sites can not offer an optimum configuration [26], since the NH_3 oxidation requires surface sites for the adsorption of two ammonia molecules and two oxygen atoms. From the surface mechanism it can be concluded that a cluster of at least five atoms is needed to form the most favorable configuration of species in a surface complex.

So far, there was no attempt in literature to incorporate the detailed surface chemistry of the ammonia oxidation in a reactor model. In most cases, the surface chemistry was approximated by a number of global steps whose rates were described by empirical rate models. For example, the experimental data were described by a first-order kinetics with respect to the surface coverage of oxygen and to ammonia pressure. The activation energy was about 125 kJ/mol in the range of ammonia partial pressures from 0.05 to 0.2 atm and at oxygen pressures ranging from 0.2 to 0.95 atm [13]. For nitrous oxide, the selectivity was proportional to the surface coverage of oxygen [13]. A problem is, however, that such equations are limited to an only relatively narrow range of reaction conditions.

The goal of this study was to develop an ammonia oxidation model which could be incorporated in an appropriate microreactor model in order to estimate the reaction rate and selectivities in case when a large axial temperature gradient is expected. This model will further be used to optimize the performance of a microreactor/heat-exchanger operating under conditions corresponding to a large adiabatic increase of temperature of the order of 1400 K [29]. The detailed reaction mechanism was obtained from the literature data and rationalized based on our experimental

results. The further kinetic model development was based on steady state and partial equilibrium approximations of the full, detailed mechanism.

An important advantage of the presented model is that it can be extended by adding new elementary steps, accounting for new effects that are considered as relevant in the high-temperature region. Also, it could be simplified for a well-defined small range of conditions by elimination of steps, less relevant during these conditions. We will show that the reaction rate and selectivities can be fit fairly well with a 13 step model with all parameters (except oxygen desorption) assumed to be functions of temperature alone. The parameters certainly contain coverage and crystal plane dependence, but our analysis suggests that most of them can be effectively lumped into constants which are functions of temperature only.

Modeling via elementary steps also allows to adapt the kinetic parameters when the catalyst state is changed. A typical example is the optimization of the activation energy of the oxygen desorption as a function of the number of atoms in a Pt cluster. It was often argued that elementary step kinetics contain so many parameters that several sets of reaction parameters can describe experimental data properly. It should be mentioned, however, that many of the individual steps were proven in independent studies that applied completely different techniques. Moreover, the orders of magnitude of rate parameters are consistent well with well-established theories.

2. Experimental

The microreactor was assembled from 14 aluminum plates, each of them containing seven semi-cylindrical microchannels of 280 μm width and 140 μm depth, 9 mm long, arranged at equal distances of 280 μm. A 25 μm alumina layer was produced in each microchannel by anodic oxidation with a 10 wt.% solution of oxalic acid [26]. Platinum impregnation was done after reactor assembly with a 1:1 solution of chloroplatinic and citric acids at room temperature. Citric acid was used as a competing agent which adsorbed in a porous layer faster than chloroplatinic acid and blocked the adsorption of the Pt precursor in the porous alumina layer. As a result, an egg-shell distribution of the Pt catalyst precursor was obtained after 6 h of impregnation. To obtain an even Pt distribution throughout the total length of the channel, the flow direction was altered every 30 min. Pt concentration in the alumina film was measured by energy-dispersive X-ray spectroscopy. Mean Pt crystallite sizes were determined from hydrogen chemisorption data by using site densities of $1.12 \times 10^{15}\,\mathrm{cm}^{-2}$ of metal [30]. The effect of the platinum loading on the catalyst activity and selectivity was investigated in [26], and the catalyst with maximum selectivity to N_2O (3.5 wt.% Pt) was chosen for the kinetic study. Based on hydrogen chemisorption data, the catalyst has a Pt dispersion of 40%, corresponding to an average particle size of 23 Å. It should be mentioned that the TOF was independent of the Pt particle size in this region.

The microstructured reactor with Pt catalyst was positioned in a specially designed reactor housing shown elsewhere [26]. The complete reactor module consists of three parts: the actual microreactor; the furnace; and the cooler. To isolate the cooler section from the microreactor, a 2 mm thick ceramic ring is positioned between the microreactor and the cooler. The temperature of the cooler was maintained at 253 K by a circulating cooling agent in order to provide the fast removal of heat produced in the reaction zone via four stainless steel screws to the cooler. The second use of the cooler is to quench the gas phase reactions and prevent further oxidation of the desired products downstream of the reactor.

Prior to the experiments, the catalyst was reduced for 1 h with H_2 at 663 K. Catalyst reduction involved first contact with flowing hydrogen (40 cm^3/min) at room temperature for 5 min. Then the temperature was raised at 2 K/min to 663 K where it was held for 1 h. At the end of the pre-treatment the entire system was purged with He and the temperature was decreased to the desired value. The ammonia, oxygen, and helium flows were set using the reactor by pass, after that the feed was diverted over the catalyst. The catalyst was pretreated in the 6 vol.% of NH_3 in oxygen mixture for 12 h before steady-state kinetic data were taken.

The reactor feed streams consisted of 2–12 vol.% NH_3 in oxygen or oxygen/He mixtures, with inlet flow rates in the range 2000–5500 N cm^3/min corresponding to contact times of 0.30–0.82 ms (Re = 151–355 at 573 K). The effluent product concentrations were measured at each temperature for 1 h at 20 min intervals. Analysis was performed by a on-line GC (HP 5890 series) equipped with Molsieve 5A and Porapak T columns and TCD detectors. The NO content of the effluent is calculated using a nitrogen mass balance. At temperatures below 553 K, when no NO was produced, the component mass balances were obtained within the accuracy of our GC analysis (5%).

3. Kinetic modeling of surface chemistry in Pt catalyzed ammonia oxidation

The reaction mechanism along with the reaction rate parameters is listed in Table 1. All the major routes along with reactions and their rate coefficients (where available) are discussed in the following paragraphs.

3.1. Dual-site mechanism

Current understanding of the ammonia oxidation reaction on platinum catalysts for surface temperatures below 673 K is that isolated sites can not offer an optimum configuration for a transition complex required for the surface interaction [22,23,26]. Furthermore, the importance of availability of oxygen vacant sites near N-containing adspecies was

Table 1
Reaction scheme and rate coefficients in form, $k = A\exp(-E/RT)\exp(\varepsilon\theta_i/RT)$

Step	Reaction	A[a]	E (kJ mol^{-1})	ε (kJ mol^{-1})	Reference
R1	$NH_3 + \{\} \rightarrow \{NH_3\}$	**2.0×10^{8}**	**0.0**	–	**[43]**
		–	112.0	–	[43]
		–	108.0	–	[44]
R2	$\{NH_3\}\rightarrow NH_3 + \{\}$	–	**96.0**	–	**[43,45]**
		1.0×10^{9}	75.2	–	[45]
		–	69.8	–	[46]
		1.3×10^{6}	0.0	–	[47]
R3	$O_2 + 2\,() \rightarrow 2\,(O)$	**2.0×10^{6}**	**0.0**	–	**[38]**
		3.3×10^{6}	0.0	–	[48]
R4	$2(O) \rightarrow O_2 + 2()$	–	**213.2**	**−60.0**	**[49]**
		–	213.2	−133.8	[50]
R5	$\{NH_3\} + (O)\rightarrow\{NH_2\} + (OH)$	**1.7×10^{15}**	**157.0**	–	**[36]**
R6	$\{NH_2\} + (O) \rightarrow \{NH\} + (OH)$	–	**0.0**	–	**[44]**
R7	$\{NH\} + (O) \rightarrow \{N\} + (OH)$	–	**0.0**	–	**[44]**
		–	58.5	–	[33]
R8	$\{N\} + (O) \rightarrow \{NO\} + ()$	–	**121.2**	–	**[33]**
R9	$\{NH\} + (O) \rightarrow \{NHO\} + ()$	–	**73.0**	–	**[51]**
R10	$\{NHO\} + (O) \rightarrow \{NO\} + (H_2O)$	–	**0.0**	–	**[51]**
		2.0×10^{15}	118.0	–	[52]
R11	$\{NO\} + () \rightarrow \{N\} + (O)$	**1.6×10^{13}**	**116.8**	–	**[21]**
			115.0	10.5	[20]
		3.0×10^{5}	79.1	–	[21]
R12	$\{N\} + \{N\} \rightarrow N_2 + 2\,\{\}$	**1.0×10^{11}**	**79.1**	–	**This study**
		1.4×10^{9}	92.9	–	[21]
R13	$\{N\} + \{NO\} \rightarrow N_2O + 2\,\{\}$	**1.0×10^{11}**	**92.9**	–	**This study**
R14	$N_2O + () \rightarrow N_2 + (O)$	**2.5×10^{8}**	**72.2**	–	**[21]**
		1.7×10^{14}	154.7	–	[19]
		–	**151.0**	–	**[43]**
R15	$\{NO\} \rightarrow NO + \{\}$	1.0×10^{16}	140.0	–	[53]
		–	139.2	−19.2	[20]
		4.3×10^{8}	54.3	–	[21]
R16	$\{NH\} + (OH) \rightarrow \{N\} + (H_2O)$	–	**46.0**	–	**[44]**
		1.0×10^{11}	79.0	−79.0	[50]
R17	$(OH) + (OH) \rightarrow (O) + (H_2O)$	–	**75.3**	–	**[54]**
		–	48.2	–	[49]
		–	**41.8**	–	**[54]**
R18	$(H_2O) + (O) \rightarrow (OH) + (OH)$	1.0×10^{11}	52.7	89.9	[50]
		–	129.6	–	[55]
R19	$(H_2O) \rightarrow H_2O + ()$	–	**40.3**	–	**[56]**
		–	41.8	–	[50]

Values in bold were used for sensitivity analysis (see Fig. 2).

[a] Pre-exponential factors of steps R1, R3, and R14 are in (s^{-1} atm^{-1}), the rest of pre-exponential factors are in (s^{-1}). Value of 1.0×10^{13} s^{-1} for the pre-exponential factors of surface steps is assumed if not otherwise mentioned.

demonstrated by the decrease of the reaction rate when a surface oxide was formed [31–33]. Finally, adsorbed oxygen did not block the ammonia adsorption [12]. All these facts led to the conclusion that a dual-site mechanism is operative. A similar conclusion on the reaction mechanism was made for ammonia oxidation on a supported ruthenium catalyst [34].

According to this mechanism, adsorbed oxygen, OH-, and H_2O-adspecies occupy the hollow sites (see Fig. 1) [35], which are called H-sites hereafter and denoted as ( ) in the mechanism. Adsorbed ammonia, and NH_2-adspecies are assumed to occupy single on-top adsorption sites [36,37]. NH- and N-adspecies occupy single bridge sites. NO-species can exist on both on top and bridge sites [38]. King et al.

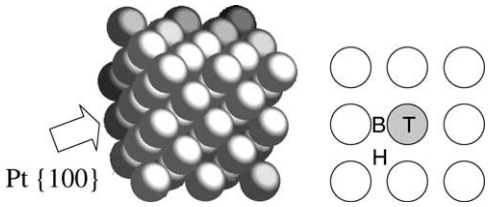

Fig. 1. Schematic view of a platinum cluster (left) and the high symmetry adsorption sites on Pt {1 0 0} (right). H, four-fold hollow site, which is called H-site and is denoted by ( ) in the kinetic model. B, bridge site; T, on-top site. The latter two types of sites are called N-sites and are denoted by { } in the kinetic model.

observed site switching during NO adsorption [39–41]: at low coverages bridge-bonded NO adspecies were formed; while at very high coverage NO switched to on-top sites due to larger repulsions between bridge-bonded molecules than between on-top molecules [40]. However, an important assumption made in the proposed mechanism is negligence of mechanistic and kinetic differences between on top and bridge sites. Both types of sites are called N-sites hereafter and are denoted by { } in the kinetic model. The assumption that these sites are equal seems appropriate because the adsorption on the bridge sites is not possible, if the on-top sites are occupied and vice versa.

Recently, it was found that NO, adsorbed on the N-site via the nitrogen atom, can reorient, possibly via a lying-down NO precursor state, to allow the O atom to come into contact with the surface on a H-site [42]. However, such process takes place under low-pressure conditions, when free H-sites exist on the surface. Under atmospheric pressure H-sites are blocked by surface species, therefore, it was assumed that NO-species adsorbed on N-sites only.

3.2. Ammonia adsorption

Ammonia adsorption (step R1, Table 1) was studied on supported platinum [57], polycrystalline platinum [58–61], and single crystal platinum planes [43,62–65]. The adsorption is similar on all Pt single crystal planes [46]. It was found that adsorption is non-activated [66], molecular [65], and ammonia was bound via the nitrogen atom [63]. For Pt {1 1 1} at 375 K, the initial sticking probability was found to be 0.8 [64], whereas for hex-R surfaces and (1 × 1) surfaces at 150 K it was about 0.9 [43]. The sticking probability was initially constant as coverage increases, but then decreases to zero. This is the classic indicator of an intrinsic precursor state, i.e. a state where a molecule is trapped above a filled site and then diffuses to an empty site in order to chemosorb [67]. Relatively large scattering of the desorption activation energy (step R2, Table 1) was reported.

3.3. Oxygen adsorption

The parameters of the dissociative adsorption (step R3, Table 1) and associative desorption of oxygen (step R4, Table 1) were also inferred from experimental data available in the literature. Due to the short distance between adsorbed atoms there is no oxygen adsorption on nearest neighbor sites. Therefore the maximum atomic oxygen coverage varies for different platinum planes. On Pt {1 1 1} planes the saturation value for atomic oxygen is 0.25 ML (1 ML = 2.47×10^{-5} mol O/m^2) [68], whereas on Pt {1 0 0} this value equals 0.63 ML [69]. After dissociation, oxygen forms $p(2 \times 2)$ islands that remain stable up to 473–503 K [70]. Recombination of oxygen occurs at a higher temperature compared to N_2 and NO formation, indicating that O is an immobile adspecies [70]. However, in the applied temperature range we assume that there is no island formation and the oxygen adsorption is restricted to one monolayer.

A number of authors take into consideration that oxygen species on the surface are not uniform with respect to bonding strength. In fact, several types of H-sites exist, e.g. three-fold H-sites on {1 1 1} surfaces and four-fold H-sites on {1 1 0} surfaces. However, according to the recent data reported by Brown et al. [71], initial heat of O_2 adsorption of 360 ± 8 kJ/mol on Pt {1 1 0} is somewhat similar to that of 316 ± 34 kJ/mol on Pt {1 1 1}. The heat of adsorption declines very rapidly on both surfaces and at the steady-state conditions reaches similar values of 145 ± 40 and 115 ± 8 kJ/mol, respectively. Therefore, we introduce one oxygen adsorption state in the kinetic model only.

Several authors considered also the short-lived energetic oxygen atoms formed by thermally activated oxygen dissociation before they equilibrate with the surface or react and, in particular, discussed the role of molecularly chemisorbed, intermediate states [72–75]. However, the lack of kinetic data concerning these species does not allow to include the molecularly chemisorbed oxygen in the kinetic model.

The sticking probability of oxygen adsorption on the Pt surface increases significantly between 500 and 600 K although it is never high [76]. Several values for the sticking coefficient of O_2 on a clean Pt {1 1 1} surface were reported in the literature, ranging from 0.02 [47] to 0.05 [48]. Walker et al. [77] reported an intermediate value of 0.03 which is virtually independent of coverage. In this study we have chosen this value as an initial guess value for a model sensitivity analysis (see Section 4).

The estimation of the activation energy of oxygen desorption was the subject of many studies, but finally a consistent value was obtained. Brennan et al. [66] found an initial value of 295 kJ/mol for polycrystalline platinum which decreased as oxygen coverage increased, due to a repulsive interaction [78–80]. For low oxygen coverages, Campbell et al. [48] obtained an activation energy for oxygen desorption from Pt {1 1 1} ranging from 213 to 176 kJ/mol; Gland and Korchak [31] reported a value of 188 kJ/mol on a stepped Pt single crystal, while Norton et al. [81] found 160 kJ/mol for oxygen on Pt {1 0 0}. For oxygen coverages close to a monolayer, Wilf and Dawson [82] reported an activation energy of 123 kJ/mol, Derry and Ross of 119 kJ/mol [83], Saliba et al. of 105 kJ/mol [79], whereas Parker et al.

found 75.5 kJ/mol [78]. The latter seems to be quoting halve the value of 153 kJ/mol reported by Wartnaby et al. [84]. It should be noted that at 0.35 ML Campbell's value of 213 kJ/mol is in good agreement with that of 215 kJ/mol reported by Wartnaby et al. [84]. The latter decreases by 62 kJ/mol at 1.0 ML. To introduce a coverage dependence of the activation energy a similar value for the energetic constant (ε, see definition in Table 1) of 60 kJ/mol was used in this study. This value was also applied in the modeling of Pt catalyzed methane combustion [49].

3.4. Ammonia activation

It is generally accepted that ammonia activation proceeds via the simple stripping of NH_3 by oxygen atoms (steps R5–R7) [32,85]. Selwyn and Lin [85] identified NH and OH as intermediate species during the course of the reaction over polycrystalline platinum. Later Mieher and Ho also observed NH_2-adspecies after the co-adsorption of O_2 and NH_3 [32]. Although the N–H bond energy varies by a factor of 10 for polycrystalline platinum and single platinum surfaces [86], surface nitrogen species (N) are more stable thermodynamically than surface imide (NH) and amide (NH_2) adspecies [87,88]. At lower temperatures, the reaction between surface oxygen and NH_3-derived species is the rate limiting reaction step as indicated by the first order of the reaction rate on oxygen partial pressure [31].

3.5. Product selectivity

It was found that the stoichiometric mixture of NH_3 and O_2 leads to preferential N_2 production for surface temperatures below 503 K [31]. The N_2 formation decreases and N_2O production increases with an inflection point as oxygen partial pressure increases. The NH_3 concentration has a minor effect on the selectivity due to the first order of the reaction rate of both nitrogen and nitrous oxide production [89]. To describe the observed kinetics, several reaction models were proposed. Fogel et al. [90] proposed a bimolecular reaction between adsorbed N and O to form NO (step R8). However, recent work on the reaction has led to a reconsideration of the mechanism involved in the NO production. Asscher et al. [33] identified two different NO formation kinetics and assigned them to different mechanisms. In addition to step R8, the formation of N_2 was attributed to the interaction between NH-adspecies and adsorbed oxygen (steps R9 and R10). NHO-adspecies were very short-lived intermediates and step R10 was much faster than step R9 [51]. It should be mentioned that step R9 was early proposed by Il'chenko and Golodets [91], who assumed that NHO-adspecies occupy two Pt sites rather than one, as proposed in [51]. Both groups considered O-adspecies coverage as the critical factor in determining the selectivitity. At relatively low oxygen coverages NO dissociates (step R11) [20,21,52]. There is no large scattering in the value of the activation energy determined for the NO dissociation. However, NO dissociation is known to be structure sensitive and therefore defect sites can facilitate this step [92,93]. Therefore, the assumption made in the end of Section 1 will lead to rate parameters which are not correct for defect sites, but only for the ratio between defect and normal sites of the used catalyst. The N_2 desorption (step R12) is fast because repulsive interactions from neighboring oxygen atoms at high oxygen coverages reduce the N_2 desorption temperature [94].

Walker et al. [77] supposed that step R13 is responsible for nitrous oxide formation. This is in agreement with the observations of Williams et al. who reported that the higher the ability to dissociate NO, the lower the selectivity toward N_2O [95,96]. Higher oxygen coverage facilitates N_2O formation, because it prevents N_2O readsorption followed by its dissociation (step R14). It also facilitates NO desorption (step R15) since the empty sites required for its dissociation are blocked [20,97]. With increasing contact time, the N_2O and NO yield decreased. This was explained by readsorption of these molecules on the catalyst surface followed by interaction with NH_x-species [13,90]. At high oxygen coverages, NH-species can also react with oxygen yielding water (step R16) [36].

To make the model complete, three other steps (steps R17–R19) describing the formation of water by reversible recombination of two OH-adspecies, followed by water desorption, were added. Thus in the kinetic model all adsorption steps follow kinetic gas theory; all other rate constants, except oxygen desorption, follow the Arrhenius law.

4. Sensitivity analysis of the kinetic model

A simulation study and a regression analysis based on the detailed reaction mechanism of Table 1 and the appropriate reactor model are very CPU time consuming. However, a simplified kinetic reaction scheme could describe the observed data correctly. It should be pointed out that the rate constants reported in literature gave a poor correlation between predicted and experimentally obtained selectivities, thus correction was required for some kinetic parameters. We substituted the unrealistically low pre-exponential factors for surface reactions R12 and R13 with a value of $10^{11}\ s^{-1}$, which is a typical value from transition state theory. In this way, the computed values were in satisfactory agreement with experimental findings for the reaction step parameters depicted in bold in Table 1.

To identify essential steps in the kinetic surface reaction scheme, a sensitivity analysis was performed. To assess the sensitivity coefficients, the rate constants of the elementary steps were multiplied by perturbation factors of 5.0 and 0.2 and the corresponding relative changes were calculated in the reaction rates and selectivities. These perturbation factors cover, in most cases, the scatter of reaction rates reported in the literature. The sensitivity coefficient was defined as

$$K_s = \frac{\ln(Y_p/Y_0)}{\ln(F)} \quad (1)$$

where Y_p and Y_0 are the concentrations of the species of interest with and without perturbation, respectively. F is the perturbation factor.

The calculations were performed for different reactor feed compositions and temperatures. While higher NH_3/O_2 ratios increased the sensitivities, the general trends were the same for all inlet mixture compositions tested. Fig. 2 shows an example (using the optimum reaction rate parameters listed in bold in Table 1) for $NH_3/O_2 = 0.068$ and catalytic wall temperatures of 548 and 698 K. The perturbation factor influences both the N_2 selectivity and NH_3 consumption rate in the same sense and has opposite influences on the N_2O selectivity. The reason for this can be easily understood when looking at the respective reaction steps: reaction steps R5–R7 lead towards N-adspecies followed by N_2 production in step R12. The increase of the rate of step R5 will increase the selectivity to N_2, thereby decreasing the selectivity towards N_2O at the same time. Therefore, while the N_2O selectivity increases, the ammonia conversion decreases and thus stabilizes the reaction system through a negative feedback between temperature and heat of reaction.

The most obvious result from the study of the kinetic parameters is that the ammonia adsorption/desorption rates are much higher than the rates of the surface reactions. As a result, steps R1 and R2 have a negligible effect on both the reaction rate and selectivities in the whole temperature range. The oxygen desorption rate does not react very sensitively to any kinetic parameter. As expected, the rate parameters of steps R6 and R7 neither influence the ammonia consumption rate, not the selectivities. This is because the reaction rates

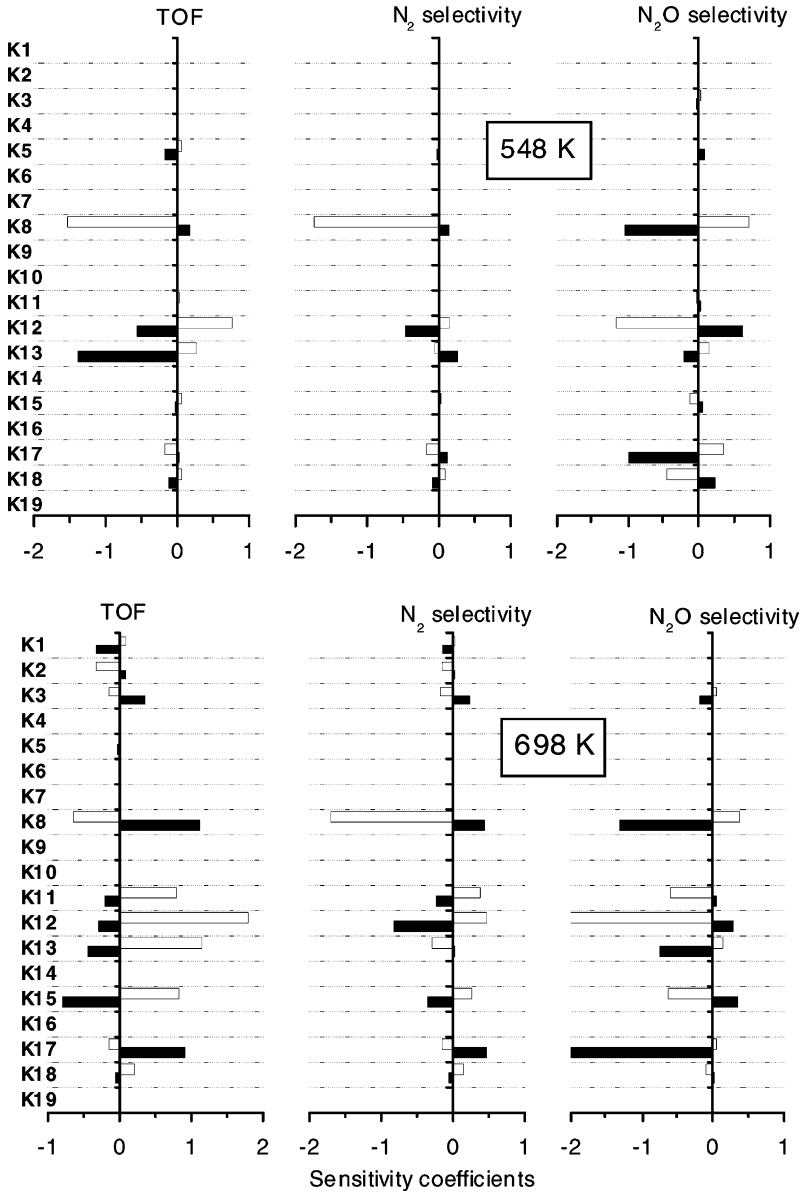

Fig. 2. Sensitivity coefficients for the TOF and the selectivity to N_2 and N_2O obtained using the reaction rate parameters listed in bold in Table 1. The $NH_3/O_2 = 0.068$, catalytic wall temperatures of 548 (above) and 698 K (below).

Table 2
Lumped reaction model for ammonia oxidation on Pt catalyst

No.	Reaction
L1	$NH_3 + \{\} \rightarrow \{NH_3\}$
L2	$\{NH_3\} \rightarrow NH_3 + \{\}$
L3	$O_2 + 2\,() \rightarrow 2\,(O)$
L4	$2\,(O) \rightarrow O_2 + 2\,()$
L5	$\{NH_3\} + 3\,(O) \rightarrow \{N\} + 3\,(OH)$
L6	$\{N\} + \{N\} \rightarrow N_2 + 2\,\{\}$
L7	$\{N\} + \{NO\} \rightarrow N_2O + 2\,\{\}$
L8	$\{NO\} + () \rightarrow \{N\} + (O)$
L9	$(OH) + (OH) \rightarrow (O) + () + H_2O$
L10	$\{N\} + (O) \rightarrow \{NO\} + ()$
L11	$H_2O + () + (O) \rightarrow (OH) + (OH)$
L12	$\{NO\} \rightarrow NO + \{\}$
L13	$N_2O + () \rightarrow N_2 + (O)$

The conditions for which the lumped model is valid, are as follows: NH_3 partial pressure, 0.01–0.12 atm; O_2 partial pressure, 0.10–0.88 atm; temperature, 400–648 K; contact time, 0.3–0.7 ms.

of these steps are also very high in comparison with that of step R5. A similar explanation follows for steps R9 and R10. The latter reaction occurs with a reaction rate which is higher than that of step R9 by several orders of magnitude. Therefore, the surface concentration of NHO adspecies is not significant. The rate of water desorption by step R19 is much higher in comparison with that for production of water in steps R10, R16, and R17. Thus, step R19 has also no impact on the parameters of interest. Finally, steps R9 and R16 of the elementary stage model do not influence the steady state of the reaction system due to very low coverages in NH-adspecies on the catalyst surface (see Section 5).

Based on these results, the lumped reaction model was obtained (Table 2). To make a distinction between the detailed model and the lumped model, index L was assigned to all reaction steps in the latter case. The lumped mechanism describes all possible surface reaction intermediates, observed during ammonia oxidation, with the exception of the intermediate adspecies NHO, NH_2, NH, and H_2O. No experimental data is available on the individual elementary steps considering the first two intermediates, and also the experiments considered here do not contain any additional information about these stages. Moreover, the surface concentrations (obtained using the final reaction rate parameters listed in Table 3) of the latter two intermediates were negligible.

Therefore, ammonia decomposition is considered as one lumped, irreversible reaction step. Although the stoichiometry of the reaction involves three oxygen surface sites, the kinetic rate law is taken to be first order in respect to oxygen surface sites, since this is a sequence of individual steps R5–R7, of which rate determining step R5 requires only one adsorbed oxygen atom. In the same way, an interaction between NH- and O-adspecies, which is a sequence of individual steps R9 and R10, was regarded as one lumped step. The kinetic rate law was also first order with respect to oxygen atoms.

5. Refinement of kinetic model parameters

To be able to optimize the kinetic parameters of the lumped model (Table 2), the surface mechanism should be included in an appropriate reactor model. The most comprehensive model is based on solving the complete Navier–Stokes equations, considering both axial and radial

Table 3
Reaction scheme with rate coefficients in form, $k = A\exp(-E/RT)\exp(\varepsilon\theta_i/RT)$

No.	Parameters[a]						
	A	$\pm\Delta A_{95\%}$	E (kJ mol^{-1})	$S_{t-95\%}$ (kJ mol^{-1})	$S_{t+95\%}$ (kJ mol^{-1})	ε (kJ mol^{-1})	Rate expression[b]
L1	**2.0×10^8**	–	**0.0**	–	–	–	$k_1 p_{NH_3}\theta_1$
L2	*1.9×10^{13}*	*0.2×10^{13}*	**96.0**	–	–	–	$k_2\theta_{NH_3}$
L3	**4.3×10^6**	–	**0.0**	–	–	–	$k_3 p_{O_2}\theta_2^2$
L4	**1.0×10^{13}**	–	**213.2**	–	–	**–60.0**	$k_4\theta_O^2$
L5	*3.0×10^{16}*	–	141.0	139.4	141.3	–	$k_5\theta_O\theta_{NH_3}$
L6	*8.0×10^{12}*	–	124.0	123.2	124.1	–	$k_6\theta_N^2$
L7	*2.5×10^{10}*	–	98.9	98.5	99.1	–	$k_7\theta_N\theta_{NO}$
L8	**1.0×10^{13}**	–	**118.0**	–	–	–	$k_8\theta_{NO}\theta_2$
L9	**1.0×10^{13}**	–	*113.0*	113.3	112.7	–	$k_9\theta_{OH}^2$
L10	*2.1×10^{13}*	–	131.0	130.7	131.2	–	$k_{10}\theta_N\theta_O$
L11	**2.0×10^8**	–	*60.5*	58.0	61.8	–	$k_{11} p_{H_2O}\theta_O$
L12	*1.5×10^{13}*	*0.2×10^{13}*	*143.0*	–	–	–	$k_{12}\theta_{NO}$
L13	**2.5×10^8**	–	*72.2*	–	–	–	$k_{13} p_{N_2O}\theta_2$

[a] Pre-exponential factors of steps L1, L3, L11, and L13 are in (s^{-1} atm^{-1}), the rest of pre-exponential factors are in (s^{-1}). Bold values were set at the values indicated in the table based on published literature data (see Table 1). They were not changed during regression analysis. Italicized values were obtained from regression analysis using the isothermal plug-flow model. They were not changed in the further optimization using the complete Navier–Stokes model. Activation energies of steps L5–L7 and L10 were found by the iteration procedure described in Section 5.3 using the complete Navier–Stokes model. The confidence intervals for activation energy were determined after parameter optimization by finding the low and high values which produce an excess sum of squared residuals corresponding to the Fisher's statistic at the 95% confidence level.

[b] $\theta_1 + \theta_{NH_3} + \theta_N + \theta_{NO} = 1$ and $\theta_2 + \theta_O + \theta_{OH} = 1$.

mass, momentum, and energy transport in each microchannel and heat conduction in the reactor material. Such model is computationally expensive, whereas it requires application of a CFD code and a supercomputer to solve it. However, depending on the flow conditions, certain approximations and simplifications can be made in representing the heat and mass transport. For example, since no diffusive terms remain, a plug-flow model is relatively simple. The plug-flow equations form a differential-algebraic equation (DAE) initial-value problem for the axial variation of the mean species composition. Furthermore, in the absence of a transverse temperature gradient across the microreactor structure, all channels behave essentially alike. Thus, only one microchannel needs to be analyzed.

5.1. The single-channel plug-flow model

The plug-flow species-continuity equations are written as:

$$\rho u A_c \frac{dY_i}{dz} - W_i A_s \dot{s}_i = 0 \quad (2)$$

where $A_c = \pi r_0^2$ is the cross-sectional area of the channel and $A_s = 2\pi r_0$ is the channel perimeter. The species mass fractions and molecular weights are given as Y_i and W_i, respectively. The molar production rate of species i by the heterogeneous reaction is represented as $\dot{s}_i$. For the present model, the plug flow is considered isothermal at the catalyst wall temperature. The regression of reaction rate constants was carried out with the ODRPACK regression program [98]. The latter is a collection of Fortran subroutines, designed to solve the orthogonal distance regression problem [99]. Points were weighted equally, and no particular points were excluded from the fitting program.

The kinetic parameters of the elementary reaction steps were determined by regression on integral data from 103 NH_3 oxidation runs over the microreactor, with NH_3 conversion, and N_2 and N_2O selectivities as the experimental responses:

$$F(1) = \frac{(2r_{L6} + r_{L13})100}{r_{L5}}, \quad \text{nitrogen selectivity(\%)} \quad (3)$$

$$F(2) = \frac{(2r_{L7} - r_{L13})100}{r_{L5}}, \quad \text{nitrous oxide selectivity(\%)} \quad (4)$$

$$F(3) = r_{L5}, \quad \text{TOF}(s^{-1}) \quad (5)$$

where r_i is the reaction rate of lumped step i.

Figs. 3 and 4 show ammonia conversion, the selectivities, and the predicted coverages of all major surface species as a function of the inlet ammonia and oxygen partial pressure, respectively. The conversion and selectivities are given at the reactor outlet and compared with the experimental data obtained. The coverages are shown at the reactor inlet. However, one can see that all coverages are constant for a

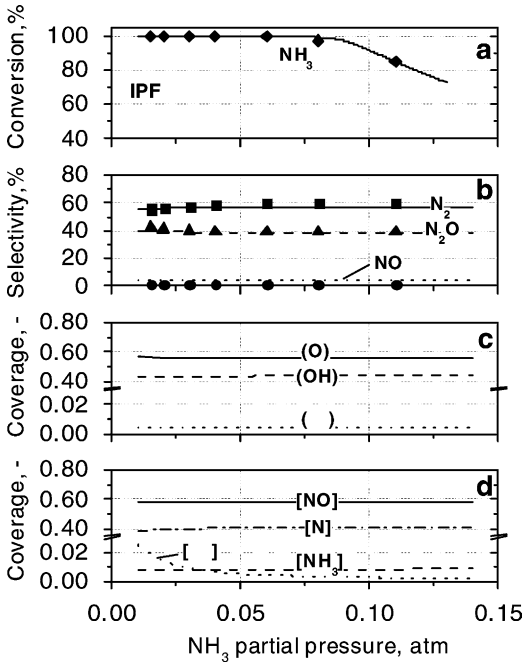

Fig. 3. (a–b) Experimental ammonia conversion and selectivities (symbols) vs. calculated according to the isothermal plug-flow (IPF) model (lines). The isothermal plug-flow model predictions of coverages on H-sites (c) and on N-sites (d) as a function of the ammonia partial pressure. Reaction conditions, O_2 = 0.88 atm; balance–He, inlet gas mixture temperature, 298 K; catalytic wall temperature, 598 K; flow rate, 3500 N cm^3/min.

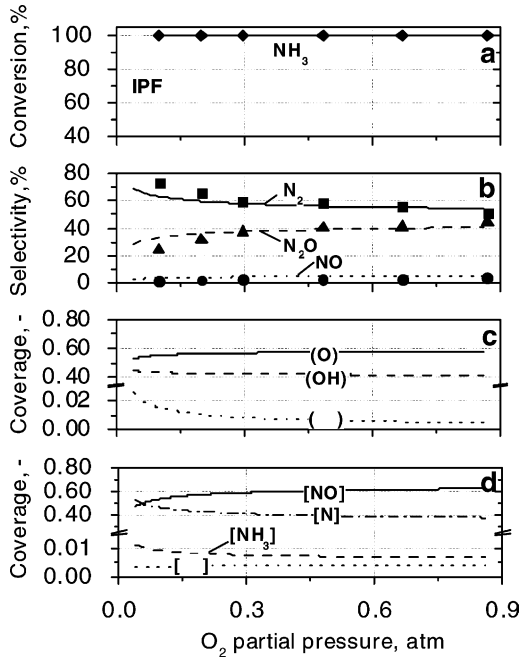

Fig. 4. (a–b) Experimental ammonia conversion and selectivities (symbols) vs. calculated according to the isothermal plug-flow (IPF) model (lines). The isothermal plug-flow model predictions of coverages on H-sites (c) and on N-sites (d) as a function of the oxygen partial pressure. NH_3 = 0.066 atm, the other conditions are the same as those in Fig. 3.

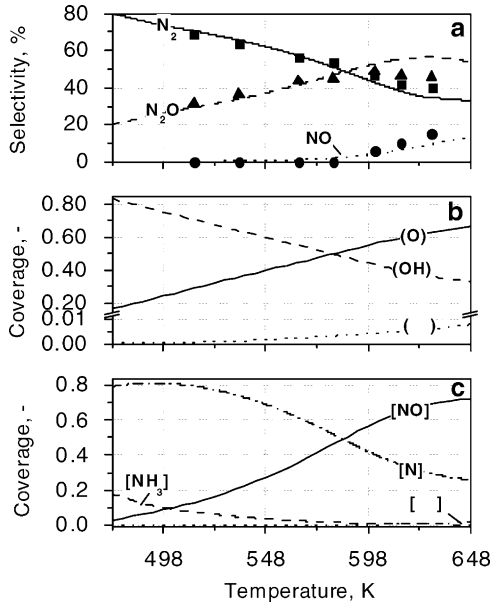

Fig. 5. (a) Experimental selectivities to nitrogen, nitrous oxide, and nitric oxide (symbols) vs. calculated according to the isothermal plug-flow (IPF) model (lines). The isothermal plug-flow model predictions of coverages on H-sites (b) and N-sites (c) sites as a function of the catalytic wall temperature. Reaction conditions, $NH_3 = 0.066$ atm; $O_2 = 0.88$ atm; flow velocity, 3500 N cm^3/min.

major part of the NH_3/O_2 ratios, therefore, they are virtually the same along the reactor axis. Considerable changes occur only at large ammonia conversions, when the ammonia partial pressure decreases below 0.01 atm. According to the surface mechanism, to obtain a high N_2O selectivity it is of importance that the coverages of NO-adspecies on the N-sites should be to some extend higher than that of N-adspecies. Such conditions can be realized at high oxygen partial pressure. On the oxygen-rich side (see Fig. 4), NO coverage is two times higher than that of N-adspecies because higher oxygen coverage on the H-sites prevents NO dissociation.

Fig. 5 illustrates the temperature dependence of both selectivities and surface coverages. Most interesting fact is the monotonous transition from an essentially OH and N covered surface, to a primary O and NO covered surface as the temperature increases. This result is in a good agreement with data obtained by Kim et al. [51], who reported that above a critical steady-state coverage of oxygen, determined by these authors as 0.2 ML, NO dissociation is inhibited. It was concluded [100,101] that step R11 was thermodynamically, not kinetically, prohibited at higher oxygen coverages due to the low heat of NO dissociative adsorption at high oxygen coverages. One can see in Fig. 5, that as the oxygen coverage reaches 0.2 ML at about 473 K, the rate of NO dissociation considerably decreased as follows from the rapid increase of the NO-species coverage. The same behavior in NO production was observed at different NH_3/O_2 ratios in the reaction mixture. Although NO production starts on the surface at temperatures of about 473 K, a high desorption activation energy prevents NO production at low temperature. It should be noted that the maximum in the N_2O selectivity was observed at a temperature which was by 50 K lower than that for the NO coverage. This fact can also be explained by the coverage dependence of N- and NO-adspecies on temperature.

In order to assess the validity of the model predictions, a comparison between the calculated reaction rate and known literature data was made in terms of the TOF at lower temperatures. The use of the TOF normalizes the difference in catalyst loading, making it possible to compare experiments with different amount of catalyst. In this way, our data obtained here were compared with results of Ostermaier et al. [22]. These authors studied ammonia oxidation over Pt catalysts with a mixture containing 1–4% NH_3 and 1–5% O_2 in helium at 413 K. Fig. 6(a) demonstrates the TOF obtained from the regression analysis of ammonia conversion data, based on the proposed kinetic mechanism. With the kinetic parameters obtained, the TOFs were calculated according to the reaction mechanism in the low temperature region at several ammonia partial pressures. The obtained values were compared with results reported by Ostermaier et al. [22] (see Table 4). Table 4 shows that the TOFs predicted by the model are in a good agreement with the published literature data. However, one can see in Fig. 6(b) that the apparent activation energy of 129.6 ± 1.2 kJ/mol, calculated according to the 13 step lumped model, exceeds both the value of 100.3 ± 8.4 kJ/mol reported for a 2.7 nm Pt crystal size catalyst [22] and that of 112.9 ± 8.4 kJ/mol found for a 15.5 nm Pt crystal size catalyst. However, our result seems to be consistent with data of Il'chenko and Golodets [102], who investigated the ammonia oxidation reaction on a Pt wire catalyst at 503 K with a 10% NH_3 in oxygen mixture at atmospheric pressure. These authors reported a reaction rate of 4.67×10^{15} molecules of $N_2 + N_2O$ cm^{-2} s^{-1}, which

Table 4
Predicted turnover frequency (TOF) vs. literature data for ammonia oxidation over supported platinum catalysts. Feed, 0.01–0.04 atm; NH_3, 0.05 atm; O_2, He balance

Temperature, K	413				433
NH_3 partial pressure, atm	0.01	0.02	0.03	0.04	0.01
TOF $\times 10^3$, s^{-1}, this study	2.5	2.5	2.5	2.5	14.8
TOF $\times 10^3$, s^{-1}, data from Ostermaier et al. [22]	2.0	2.1	2.3	2.4	9.0

Data from Ostermaier et al. [22] are for unsintered 1 wt.% Pt catalyst (crystal size: 2.7 nm). Accuracy of these data: ±10%.

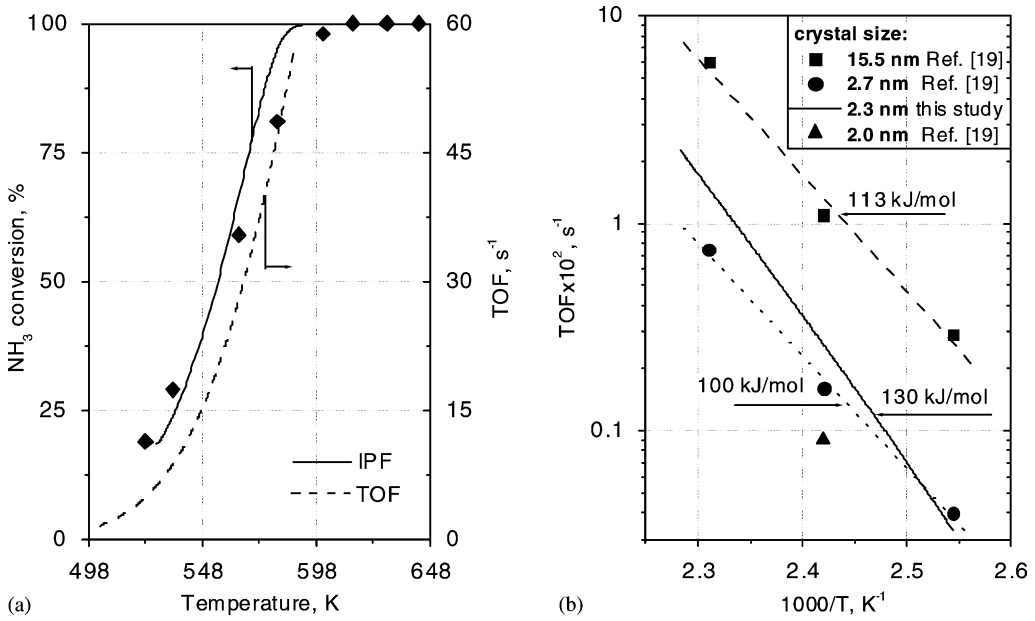

Fig. 6. (a) Experimental ammonia conversion (symbols) vs. calculated (solid line) according to the isothermal plug-flow (IPF) model as a function of catalytic wall temperature. Corresponding turnover frequencies (TOF, dashed line) are given for comparison. The reaction conditions are the same as those in Fig. 5. (b) The 13-step kinetic model predictions vs. literature data [22] obtained on Pt catalysts with a different particle size for $T < 435$ K.

corresponds to a TOF of 6.2 mol NH_3/(s mol Pt), using a platinum site density of 1.5×10^{15} cm^{-2} [68]. This is still 3.9 times larger than the TOF value of 1.6 ± 0.1 s^{-1} predicted by the 13 step lumped model at the same temperature. However, it does not mean that our model underestimates the reaction rate, because such difference can be explained by structure sensitivity of this reaction [22,23].

In general, the model predictions show a rather good agreement both with published literature data and our experimental results for ammonia partial pressures above 0.03 atm. This level of agreement, over a temperature interval of above 250 K, provides considerable support of the obtained kinetic parameters.

However, as the ammonia partial pressure decreases, nitrogen selectivity is slightly underpredicted. This appears to be due to considerable deviation of the catalyst temperature from isothermal conditions assumed in the plug-flow model. The heat produced by the reaction was not enough to maintain the desired temperature at the very high flow rates of the reagent mixture, which was fed at room temperature. Another difference between modeling and experiment is that the plug-flow model overestimates ammonia conversion at higher temperatures (see Fig. 6(a)). This is an anticipated result, since the inherent radially homogeneous nature of the plug-flow model imposes more intimate interaction between the gas and the surface. In reality, a boundary layer inhibits mass transfer and therefore mass-transfer limitations have to be considered due to the extremely high reaction rate (TOF >50 s^{-1}, see Fig. 6(a)) at elevated temperatures. Both these phenomena are discussed in the following section.

5.2. Plug-flow model validation

The plug-flow model assumes that there are no radial variations in the species composition. The significance of gas–solid interface mass-transfer limitations was ruled out based on the calculation of the Damköhler number. We demonstrated in [26] that Da < 0.3 under all reaction conditions where the temperature was below 573 K.

An important assumption, that could lead to differences in predicted and experimental reaction rates and selectivities, is the constant catalyst temperature along the reactor axis. The validity of this assumption can be rationalized by comparing isothermal and non-isothermal plug-flow (NIPF) models. In the latter case, the temperature profile can be approximated by a second order polynomial function (6) obtained from the complete Navier–Stokes simulation (see Section 5.3) at ammonia and oxygen inlet partial pressures of 0.066 and 0.88 atm, respectively:

$$T(z) = 578 + 4.99 \times 10^3 z - 4.31 \times 10^5 z^2 (\mathrm{K}) \quad (6)$$

where z is the axial coordinate in meters. Fig. 7 shows a comparison between simulation results for the isothermal (IPF) and NIPF models for a gas inlet temperature of $T_{in} = 298$ K. As seen in Fig. 7(a), the ammonia gas phase concentration agrees well between isothermal and non-isothermal solutions over the entire length of the reaction channel, while the results for selectivity deviate substantially more for these two cases (see Fig. 7(b)). Especially, in the first millimeter of the channel length a difference in the N_2 and N_2O selectivities as high as 10% was observed demonstrating that the isothermal plug-flow model can only give initial

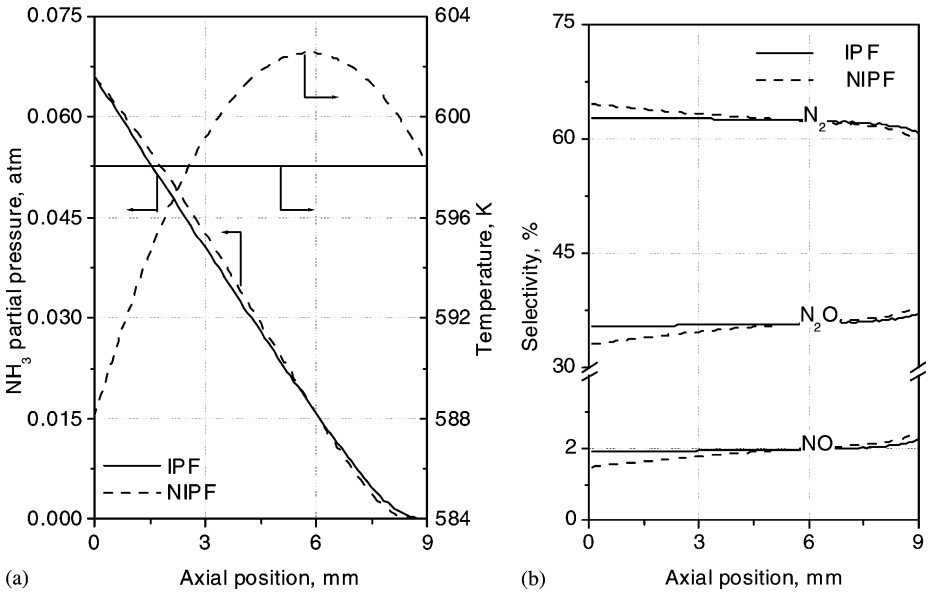

Fig. 7. Comparison of the axial profiles of temperature and ammonia gas phase concentration (a) and selectivities (b) for the isothermal (IPF) and non-isothermal plug-flow (NIPF) models. Selectivities to nitrogen and nitrous oxide were calculated by Eqs. (3) and (4), respectively. Selectivity to nitric oxide was calculated as follow: SNO = 100 × L12/L5. Inlet conditions are the same as those in Fig. 5.

guess values of the kinetic parameters suitable for further optimization by solving the complete Navier–Stokes model.

5.3. Complete Navier–Stokes model

Here the Navier–Stokes equations [103] assume perfect-gas behavior and laminar flow. Their solution predicts the axisymmetric velocity, pressure, temperature, and species-composition fields in the reaction channel. The complete Navier–Stokes model was solved using the FLUENT® software [104], using its user-subroutine interfaces to specify the heterogeneous chemical-reaction mechanism on the channel walls. The FLUENT® software implements a finite-volume approach [105]. About 2 h of CPU time (CRAY Origin 2000 supercomputer) were needed for solution convergence. The simulation was based on the three-dimensional geometry of a single reactor plate. The Navier–Stokes solutions are determined on a non-uniform mesh having 124 axial and 21 radial elements. The radial mesh is concentrated near the channel walls. The axial mesh is concentrated near the beginning of the channel. This choice of meshing places the highest mesh concentration in the regions expected to have the largest gradients in the solution. A mesh refinement study confirmed that these choices for meshing lead to mesh-independent results.

In order to compare the NIPF and Navier–Stokes solutions, in the latter case the heat transfer coefficient for heat losses to the environment was fitted to obtain an average temperature at the outer surface of the microchannel equal to that in the plug-flow model. The average temperature of the outer surface was extracted from simulations using the following area average:

$$\bar{T}_{\text{surf}} = \frac{\int_A T(A)\,\mathrm{d}A}{\int_A \mathrm{d}A} \tag{7}$$

The outer wall of the reaction channel was considered as a conducting wall with the heat conductivity of aluminum ($\lambda = 240\,\text{W/m K}$), whereas the inner wall was considered as a conducting wall with the heat conductivity of alumina ($\lambda = 1.0\,\text{W/m K}$). The reactions on the catalytic surface of the reaction channel were used as a boundary condition for the gas phase chemical species. The catalyst temperatures were fitted with a heat transfer coefficient for heat losses to the environment in the range of (3–15) × $10^3\,\text{W/m}^2\,\text{K}$. For the reaction rate constants, the values found by the ODRPACK routine for the NIPF model were used.

To compare two solutions, it is necessary to determine the mass-weighted radially averaged species compositions (8) at a given axial location from the Navier–Stokes solution:

$$Y_i = \frac{\int_0^R \rho u Y_i r\,\mathrm{d}r}{\int_0^R \rho u r\,\mathrm{d}r} \tag{8}$$

Fig. 8 illustrates that at temperatures below 573 K, there is no difference between the non-isothermal plug flow and the complete Navier–Stokes models confirming that the reagent consumption rates at these conditions are actually limited by surface reactions rather than by external mass transfer through a boundary layer. At higher temperatures, however, the plug-flow model predicts a more rapid ammonia consumption and also substantially overestimates the N_2O selectivity. This becomes more obvious if we compare the NH_3

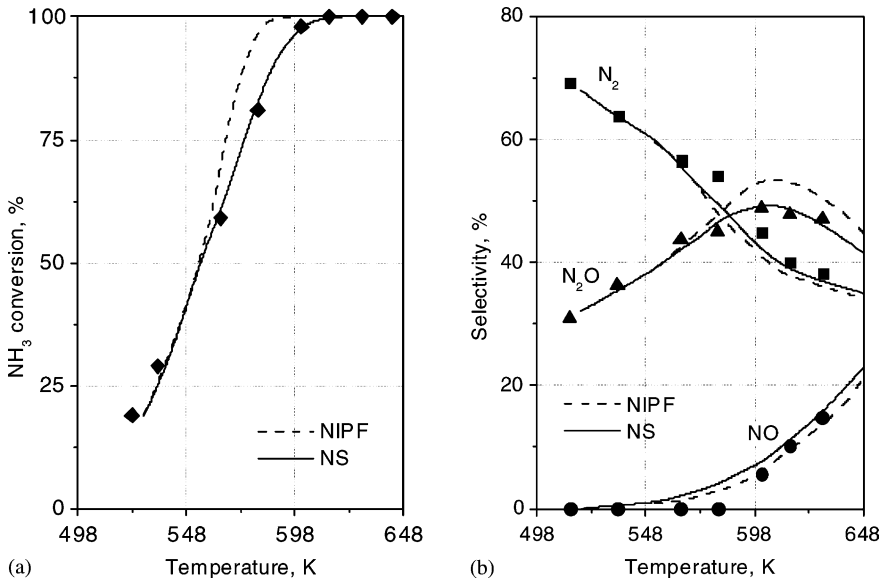

Fig. 8. Comparison of ammonia conversion (a) and selectivities (b) to N_2 and N_2O between the complete Navier–Stokes (NS) model and the non-isothermal plug-flow (NIPF) model. Symbols represent the experimental data. Inlet conditions are the same as those in Fig. 5.

conversion and selectivity profiles along the length of the reactor (see Fig. 9). One can see that after the formation of the boundary layer, selectivity to N_2O increases much slower than predicted by the plug-flow model. The nitrogen selectivities predicted by both models are in rather good agreement at the end of the channel. However, if the selectivities in Fig. 8 were to be compared in the immediate vicinity of the catalyst leading edge, there would also be a rather large difference in the N_2 selectivity between the models.

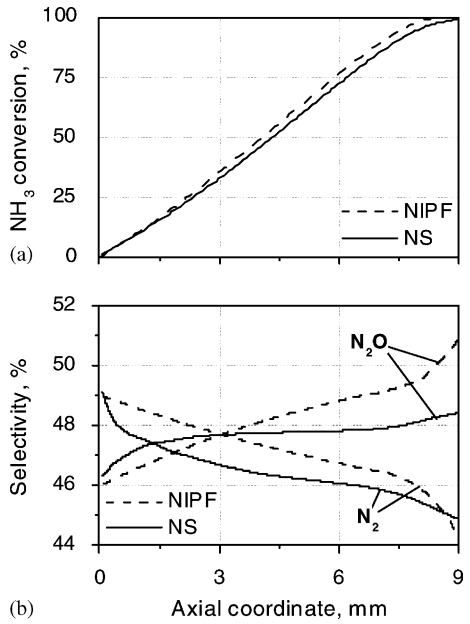

Fig. 9. Comparison of the axial profiles of ammonia conversion (a) and selectivities (b) to N_2 and N_2O for the non-isothermal plug-flow model (NIPF) and complete Navier–Stokes (NS) model. Inlet gas mixture temperature, 298 K; average catalytic wall temperature, 598 K. The other conditions are the same as those in Fig. 8.

Therefore, the kinetic parameters obtained by the NIPF model had to be adapted, so that the Navier–Stokes solution fits the experimental data properly in the whole range of temperatures and contact times. The sensitivity analysis showed that four kinetic parameters might be of relevance here: the rate constants of reaction steps L5, L6, L7, and L10. The activation energies of these steps were optimized in the FLUENT® simulations. The pre-exponential factors of these steps as well as the remaining kinetic parameters were used as found by the ODRPACK routine.

The finite difference method was applied for adapting the kinetic parameters with the Navier–Stokes model. In this technique, each of the reaction parameters was systematically modified. Because of the negative feedback between the activation energy of step L7 and the N_2O selectivity, the former was decreased by 1% and a set of simulations was performed with the new values of the activation energies (E_{ai0}) of steps L5, L6, and L10. These values were adapted, depending on the sensitivity coefficient, as follows:

$$E_{ai} = E_{ai0} \pm 0.01\frac{E_{ai0}}{K_s} \quad (9)$$

where E_{ai} and E_{ai0} are the new and old values of the activation energy and K_s is the sensitivity coefficient for the N_2O selectivity (see Section 4). The sum of the mean-square deviations of the N_2, N_2O selectivities and NH_3 conversion from experimental data was chosen as an objective function. The gradient of the objective function with respect to the selected kinetic parameters was evaluated. The gradient is used during optimization to calculate a search direction using steepest descent method. The gradient components are

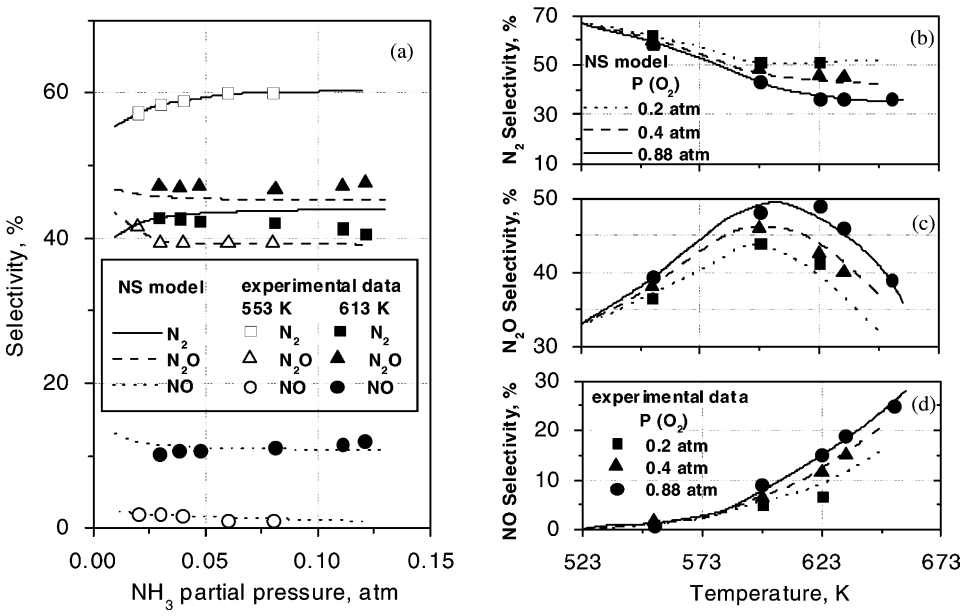

Fig. 10. Experimental data vs. simulation results obtained with the complete Navier–Stokes (NS) model: (a) selectivity to all end products as a function of the ammonia partial pressure, $O_2 = 0.88$ atm, inlet gas mixture temperature, 298 K, flow velocity, 3500 N cm^3/min; (b–d) selectivity to nitrogen (b); nitrous oxide (c); and nitric oxide (d) as a function of an average catalytic wall temperature for three different oxygen partial pressures. $NH_3 = 0.066$ atm.

obtained by independently perturbing each kinetic parameter with a finite step, calculating the corresponding value of the objective function using CFD analysis, and forming the ratio of the differences. After finding the minimum of the objective function along the search direction, the entire process is repeated until convergence is reached. The optimized parameters for the lumped reaction mechanism are listed in Table 3. It should be noted that if the starting parameter estimates based on the plug-flow model had not been available, the task of data fitting of our results would have been much more difficult. Finding starting estimates for the rate parameters in such rate models remains a major problem.

The comparison between experimental data and predicted selectivities is shown in Fig. 10. The optimum in N_2O selectivity is found at about 598 K. The observed increase of the N_2O selectivity with increasing oxygen/ammonia ratio can be rationalized by a composition effect, where the increasing oxygen supply will eventually favor the formation of NO-adspecies on the surface. Moreover, a temperature effect decreases the hot-spot temperature in the channel, because the oxygen-rich mixture has larger heat capacity. One can see that, despite the remaining deviations, the simulations show generally a close agreement with the experimental data, indicating that the model describes the essential steps in the mechanism correctly.

Fig. 11 demonstrates that gas phase and catalyst surface are thermally equilibrated within 5% after roughly 6 mm in the reactor. In the front part of the microchannel, the catalyst temperature is about 200 K higher than the temperature of the gas phase due to the relatively high thermal conductivity of the solid and the high flow rate of the feed gases. Between the entrance and the exit of the microchannel, a temperature difference of about 15 K is established due to higher rates of exothermic reactions in the latter parts of the channel. As mentioned, the catalytic wall temperature profile obtained here was used in the NIPF model (see Eq. (6)).

Finally, some typical results on the effect of contact time are presented in Fig. 12. It should be noted that the temperature profile changes considerably from that described by

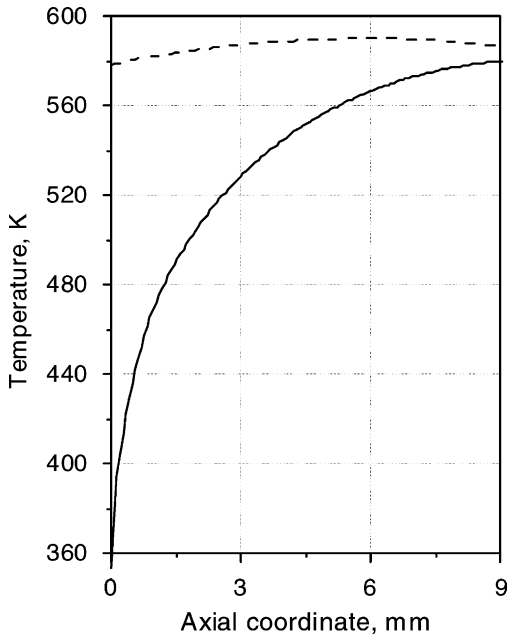

Fig. 11. Predictions of the complete Navier–Stokes model for gas-phase (solid line) and catalytic wall (dashed line) temperatures along the axial reactor coordinate. Inlet conditions are the same as those in Fig. 7.

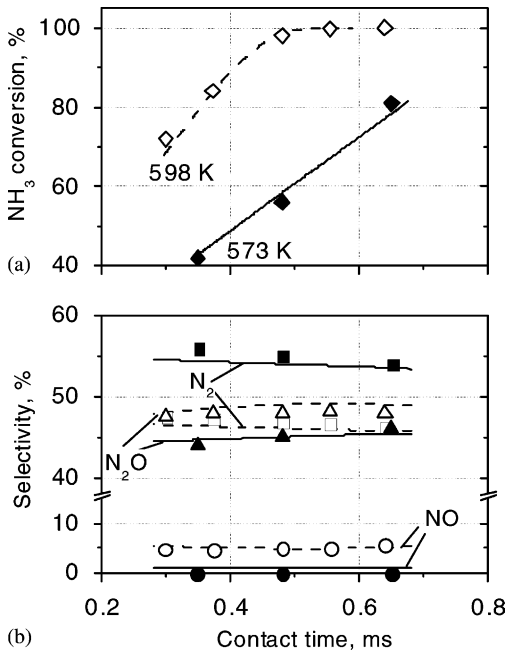

Fig. 12. Experimental (symbols) ammonia conversion (a) and selectivity (b) vs. calculated according to the complete Navier–Stokes model (lines) as a function of the contact time. Closed symbols are given for 573 K, open symbols are given for 598 K. Inlet conditions, $NH_3 = 0.066$ atm; $O_2 = 0.88$ atm; gas mixture temperature, 298 K; average catalytic wall temperature, 598 K.

Eq. (6) with increasing or decreasing flow velocity. Experimental data obtained at higher or lower contact times were not included in the regression analysis. However, to estimate the range of validity of the model predictions we also should compare the simulated results with data obtained at different residence times. As was shown by sensitivity analysis, step R14 has little impact on the product distribution because its characteristic time of 390 ms (TOF $\sim 2.5\,s^{-1}$ at 600 K) is much longer than the residence time under chosen reaction conditions (<1 ms). Therefore, as long as the residence time is kept low enough, no considerable changes in selectivity due to the nitrous oxide readsorption/decomposition (step L13) can be expected. Fig. 12 shows that the measured ammonia conversions and selectivity are in satisfactory agreement with those predicted through the application of the complete Navier–Stokes model.

6. Conclusions

This work shows that it is feasible to investigate the reaction kinetics of fast, strongly exothermic reactions at very small time and length scales. The developed microreactor set-up provides very fast heat transfer from the reaction zone to a quench section which enables the study of the reaction in an integral reactor approaching near isothermal conditions. As an example, the low temperature kinetics of the ammonia oxidation over a supported platinum catalyst in a microstructured reactor was studied. A dual-site surface reaction mechanism was developed which takes into consideration different adsorption sites for oxygen and nitrogen-containing adspecies. The sensitivity analysis results demonstrated that there are only five major surface reaction steps that influence the reaction rate and selectivity. After elimination and combination of several elementary steps, a lumped reaction model was obtained. The model incorporates a 13 step reaction mechanism, which is combined with a plug-flow model. A regression analysis performed against experimental data resulted in a set of reaction parameters which successfully predicts a wide range of experimental data below 573 K. However, above 573 K the ammonia conversion and N_2O selectivity were overestimated for all NH_3/O_2 ratios. Combining the flow characteristics of the reaction mixture and the heat evolution in the course of the reaction by means of the FLUENT® code with the surface mechanism included, resulted in much better agreement between the model and experiment. The model obtained will be used further to design a microstructured reactor/heat-exchanger operating at conditions corresponding to an adiabatic temperature rise of about 1400 K.

References

[1] O. Wörz, Microreactors as tools in chemical research, in: Proceedings of the 5th International Conference on Microreaction Technology, Strasbourg, France, 2001, p. 83.
[2] P. Claus, D. Hönicke, T. Zech, Catal. Today 67 (2001) 319.
[3] S. Walter, E. Joannet, M. Schiel, I. Boulett, R. Philipps, M.A. Liauw, Microchannel reactor for the partial oxidation of isoprene, in: Proceedings of the 5th International Conference on Microreaction Technology, Strasbourg, France, 2001, p. 85.
[4] D.A. Frank-Kamenetskii, Zh. Teor. Phiz. 9 (1939) 1457.
[5] W.I. Curless, G.A. Terry, US Patent 3,360,336 (1967).
[6] N.I. Il'chenko, Rus. Chem. Rev. 45 (1976) 1119.
[7] J.E. DeLaney, W.H. Manogue, The effect of catalyst sintering on low temperature ammonia oxidation over supported platinum, in: J.W. Hightower (Ed.), Proceedings of the 5th International Conference on Congress on Catalysis, Vol. 1, Elsevier, Amsterdam, 1973, p. 267.
[8] Y. Li, J.N. Armor, Appl. Catal. B 13 (1997) 131.
[9] Ya.M. Fogel, B.T. Nadykto, V.F. Rybalko, V.I. Shvachko, I.E. Korobchanskaya, Kinet. Katal. 5 (1964) 496.
[10] C.W. Nutt, S.W. Kapur, Nature 220 (1968) 697.
[11] C.W. Nutt, S.W. Kapur, Nature 224 (1969) 169.
[12] T. Pignet, L.D. Schmidt, J. Catal. 40 (1975) 212.
[13] N.I. Il'chenko, G.I. Golodets, I.M. Avilova, Teor. Exp. Khim. 11 (1975) 56.
[14] J.L. Gland, V.N. Korchak, J. Catal. 53 (1978) 9.
[15] J.L. Gland, G.C. Woodward, J. Catal. 61 (1980) 543.
[16] H. Bosch, F. Janssen, Catal. Today 2 (1988) 369.
[17] F. Janssen, R. Meier, Catal. Today 16 (1993) 157.
[18] V.I. Parvulescu, P. Grange, B. Delmon, Catal. Today 46 (1998) 233.
[19] R.J. Gorte, L.D. Schmidt, J.L. Gland, Surf. Sci. 109 (1981) 367.
[20] G. Pirug, H.P. Bonzel, J. Catal. 50 (1977) 64.
[21] R.R. Sadhankar, D.T. Lynch, Ind. Eng. Chem. Res. 36 (1997) 4609.
[22] J.J. Ostermaier, J.R. Katzer, W.H. Manogue, J. Catal. 33 (1974) 457.
[23] W.H. Manogue, J.R. Katzer, J. Catal. 32 (1974) 166.
[24] J.J. Ostermaier, J.R. Katzer, W.H. Manogue, J. Catal. 41 (1976) 277.
[25] G.R. Wilson, W.K. Hall, J. Catal. 24 (1972) 306.
[26] E.V. Rebrov, M.H.J.M. de Croon, J.C. Schouten, Catal. Today 69 (2001) 183.

[27] K. Otto, H.C. Yao, J. Catal. 66 (1980) 229.
[28] O.M. Poltorak, V.S. Boronin, Zh. Fiz. Khim. 40 (1966) 1436.
[29] E.V. Rebrov, M.H.J.M. de Croon, J.C. Schouten, Design of a cooled microreactor for platinum catalyzed ammonia oxidation, in: M. Matlosz, W. Ehrfeld, J.P. Baselt (Eds.), Proceeding. 5th International Conference on Microreaction Technology, IMRET 5, Strasbourg, France, May 27–30, Springer, 2001, p. 49.
[30] L. Spenadel, M. Boudart, J. Phys. Chem. 64 (1960) 204.
[31] J.L. Gland, V.N. Korchak, J. Catal. 53 (1978) 9.
[32] W.D. Mieher, W. Ho, Surf. Sci. 322 (1995) 151.
[33] M. Asscher, W.L. Guthrie, T.-H. Lin, G.A. Somorjai, J. Phys. Chem. 88 (1984) 3233.
[34] T.J. Schriber, G. Parravano, Chem. Eng. Sci. 22 (1967) 1067.
[35] J.M. Bradley, A. Hopkinson, D.A. King, J. Phys. Chem. 99 (1995) 17032.
[36] D.A King, in: G.F. Froment, K.C. Waugh (Eds.), Dynamics of Surfaces and Reaction Kinetics in Heterogeneous Catalysis, Elsevier, Amsterdam, 1997, p. 79.
[37] N. Materer, U. Starke, A. Barbieri, R. Döll, K. Heinz, M.A. van Hove, G.A. Somorjai, Surf. Sci. 325 (1995) 207.
[38] R.J. Gorte, J.L. Gland, Surf. Sci. 102 (1981) 348.
[39] W.A. Brown, Q. Ge, R.K. Sharma, D.A. King, Chem. Phys. Lett. 299 (1999) 253.
[40] W.A. Brown, R.K. Sharma, D.A. King, J. Phys. Chem. B 102 (1998) 5303.
[41] Q. Ge, W.A. Brown, R.K. Sharma, D.A. King, J. Chem. Phys. 110 (1999) 12082.
[42] W.A. Brown, D.A. King, J. Phys. Chem. B 104 (2000) 2578.
[43] J.M. Bradley, A. Hopkinson, D.A. King, Surf. Sci. 371 (1997) 255.
[44] A. Fahmi, R.A. van Santen, Zeitschrift für Physikalische Chemie, Bd. 197 R, Oldenbourg Verlag, München, 1996, p. 203.
[45] J.M. Gohndrone, C.W. Olsen, A.L. Backman, T.R. Gow, E. Yagasaki, R.I. Masel, J. Vac. Sci. Technol. A 7 (1989) 1986.
[46] D.G. Löffler, L.D. Schmidt, J. Catal. 41 (1976) 440.
[47] G.A. Somorjai, Introduction to Surface Chemistry and Catalysis, Wiley, New York, 1994.
[48] C.T. Campbell, G. Ertl, H. Kuipers, J. Segner, J. Surf. Sci. 107 (1981) 220.
[49] O. Deutschmann, L.I. Maier, U. Riedel, A.H. Stroemman, R.W. Dibble, Catal. Today 59 (2000) 141.
[50] Y.K. Park, P. Aghalayam, D.G. Vlachos, J. Phys. Chem. A 103 (1999) 8101.
[51] M. Kim, S.J. Pratt, D.A. King, J. Am. Chem. Soc. 122 (2000) 2409.
[52] T. Fink, J.-P. Dath, M. Basset, R. Imbihl, G. Ertl, Surf. Sci. 245 (1991) 96.
[53] L.D. Schmidt, J.L. Gland, Surf. Sci. 109 (1981) 367.
[54] A.B. Anton, D.C. Cadogan, J. Vac. Sci. Technol. 9 (1991) 1890.
[55] W.R. Williams, C.M. Marks, L.D. Schmidt, J. Phys. Chem. 96 (1992) 5922.
[56] P.A. Thiel, T.E. Madey, Surf. Sci. Rep. 7 (1987) 211.
[57] B.A. Morrow, I.A. Cody, J. Catal. 45 (1976) 151.
[58] A.J.B. Robertson, E.M.A. Willhoft, Trans. Faraday Soc. 63 (1967) 476.
[59] D.G. Löffler, L.D. Schmidt, J. Catal. 41 (1976) 490.
[60] M.J. Mummey, L.D. Schmidt, Surf. Sci. 91 (1980) 301.
[61] G.A. Papapolymerou, L.D. Schmidt, Langmuir 1 (1985) 488.
[62] G.B. Fisher, Chem. Phys. Lett. 79 (1981) 452.
[63] B.A. Sexton, G.E. Mitchell, Surf. Sci. 99 (1980) 523.
[64] W.L. Guthrie, J.D. Sokol, G.A. Somorjai, Surf. Sci. 109 (1981) 390.
[65] J.L. Gland, J. Kollin, Surf. Sci. 104 (1981) 478.
[66] D. Brennan, D.O. Hayward, B.M.W. Trapnell, Proc. R. Soc. A 256 (1960) 81.
[67] P. Kisliuk, J. Phys. Chem. Solids 3 (1957) 95.
[68] N.R. Avery, Chem. Phys. Lett. 96 (1983) 371.
[69] K. Griffiths, T.E. Jackman, T.A. Davies, P.R. Norton, Surf. Sci. 138 (1984) 113.
[70] J.L. Gland, E.B. Kollin, J. Chem. Phys. 107 (1997) 6443.
[71] W.A. Brown, R. Kose, D.A. King, Chem. Rev. 98 (1998) 797.
[72] J.E. Davis, C.B. Mullins, Surf. Sci. 380 (1997) L513.
[73] A.C. Luntz, M.D. Williams, D.S. Bethune, J. Chem. Phys. 89 (1988) 4381.
[74] C.T. Rettner, C.B. Mullis, J. Chem. Phys. 94 (1991) 1636.
[75] X.-C. Guo, J.M. Bradley, A. Hopkinson, D.A. King, Surf. Sci. 310 (1994) 163.
[76] X.-C. Guo, J.M. Bradley, A. Hopkinson, D.A. King, Surf. Sci. Lett. 292 (1993) L786.
[77] A.V. Walker, M. Gruyters, D.A. King, Surf. Sci. 384 (1997) L791.
[78] D.H. Parker, M.E. Bartram, B.E. Koel, Surf. Sci. 217 (1989) 489.
[79] N.A. Saliba, Y.-L. Tsai, C. Panja, B.E. Koel, Surf. Sci. 419 (1999) 79.
[80] G.W. Coulston, G.L. Haller, J. Chem. Phys. 95 (1991) 6932.
[81] P.R. Norton, K. Griffiths, P.E. Bindner, Surf. Sci. 138 (1984) 125.
[82] M. Wilf, P.T. Dawson, Surf. Sci. 65 (1977) 399.
[83] G.N. Derry, P.N. Ross, Surf. Sci. 140 (1984) 165.
[84] C.E. Wartnaby, A. Stuck, Y.Y. Yeo, D.A. King, J. Phys. Chem. 100 (1996) 12483.
[85] G.S. Selwyn, M.C. Lin, Langmuir 1 (1985) 212.
[86] D.G. Löffler, L.D. Schmidt, Surf. Sci. 59 (1976) 195.
[87] N. Cohen, K.R. Westberg, J. Phys. Chem. Ref. Data 20 (1991) 1211.
[88] G.S. Selwyn, G.T. Fujimoto, M.C. Lin, J. Phys. Chem. 86 (1982) 760.
[89] J. Schmidt, M. Shentuch, Chem. Eng. Commun. 46 (1986) 289.
[90] Ya.M. Fogel, P.T. Nadykto, V.I. Shvachko, V.F. Rybalko, I.E. Korobchanskaya, Kinet. Katal. 5 (1964) 942.
[91] N.I. Il'chenko, G.I. Golodets, Teor. Experim. Khim. 9 (1973) 36.
[92] J.L. Gland, Surf. Sci. 71 (1978) 327.
[93] W.F. Banholzer, Y.O. Park, K.M. Mak, R.I. Masel, Surf. Sci. 128 (1983) 176.
[94] K. Schwaha, E. Bechtold, Surf. Sci. 91 (1980) 187.
[95] A.A. Tolia, Ch.T. Williams, Ch.G. Takoudis, M.J. Weaver, J. Phys. Chem. 99 (1995) 4599.
[96] Ch.T. Williams, A.A. Tolia, H.Y.H. Chan, Ch.G. Takoudis, M.J. Weaver, J. Catal. 163 (1996) 63.
[97] H.P. Bonzel, G. Pirug, Surf. Sci. 62 (1977) 45.
[98] P.T. Boggs, R.H. Byrd, J.R. Donaldson, R.B. Schnabel, ACM Trans. Math. Software 15 (1989) 348.
[99] P.T. Boggs, J.E. Rogers, Contemporary Math. 112 (1990) 183.
[100] L. Vattuone, Y.Y. Yeo, D.A. King, J. Chem. Phys. 104 (1996) 8096.
[101] L. Vattuone, Y.Y. Yeo, D.A. King, Catal. Lett. 41 (1996) 119.
[102] N.I. Il'chenko, G.I. Golodets, J. Catal. 39 (1975) 73.
[103] L.L. Raja, R.J. Kee, O. Deutschmann, J. Warnatz, L.D. Schmidt, Catal. Today 59 (2000) 47.
[104] FLUENT® Version 4.5, FLUENT Inc., Lebanon, New Hampshire, 1999.
[105] S.V. Patankar, Numerical Heat Transfer and Fluid Flow, McGraw-Hill, New York, 1980.